Experiment Based Superposition Thermal Modeling of Laser Powder Bed Fusion

Cody S. Lough[1,2], Robert G. Landers[2], Douglas A. Bristow[2],
James A. Drallmeier[2], Ben Brown[1], Edward C. Kinzel[3]

[1]Kansas City National Security Campus*, Kansas City, MO 64147

[2]Department of Mechanical and Aerospace Engineering, Missouri University of Science and Technology, Rolla, MO 65409

[3]Department of Aerospace and Mechanical Engineering, University of Notre Dame, Notre Dame, IN 46556

*The Department of Energy's Kansas City National Security Campus is operated and managed by Honeywell Federal Manufacturing & Technologies, LLC under contract number DE-NA0002839.

Abstract

This paper evaluates experiment-based superposition thermal modeling for Laser Powder Bed Fusion (LPBF) with a pulsed laser. An analytical pulsed laser thermal model establishes the modeling procedure. The framework inverts a powder bed's single pulse temperature response from experimental spatiotemporal Short-Wave Infrared (SWIR) camera data. Superimposing this response along a scan path simulates multi-pulse LPBF. Results show the experimentally informed superposition model rapidly and accurately predicts a layer's temperature history. The model has applications in correction of thermally driven LPBF errors and in-situ part qualification.

Introduction

Laser Powder Bed Fusion (LPBF) fabricates high resolution, complex, metal parts layer-by-layer. Part geometry variances and changing laser scan pathing drive thermal differences within layers that produce defects [1]. Analytical [2], numerical [3], and high fidelity [4] thermal models aim to understand LPBF's underlying physics causing those variations with significant computational expense. Controls-oriented superposition thermal models quickly predict a layer's temperature history. The superposition approach's linear assumptions reduce a layer's computation time from days, or weeks, to minutes, making it feasible for application in real-time process correction.

Moran et al. combined Rosenthal's moving point heat source solution with FEA to perform superposition simulations of a laser scanning Ti-6Al-4V [5]. Moran et al. found their model provides results accurate to FEA only simulations with a significant decrease in computation time. The computation time reduction makes large scale simulations practical. Schwalbach et al. used Green's function methodology to develop a thermal model for LPBF with a continuous wave (CW) laser [6]. Schwalbach et al.'s model approximates a scanning CW laser by superimposing the temperature response from distinct heat sources seeded along the raster path. Schwalbach et al. demonstrated their model's temperature results agree with analytical solutions, calibration provides accurate melt pool dimension predictions, and the approach indicates thermal history spatial variations.

Temperature and state dependent thermal properties, latent heat effects from melting and solidification, and material vaporization make the LPBF process highly non-linear. This limits analytical superposition models to qualitatively predicting part geometry-scan path interaction effects. A superposition model informed by thermal camera data would provide quantitative predictions with LPBF's physics embedded, but this requires the experimental measurements to behave linearly. The quantitative analysis may improve decision making capability, and baseline in-situ measurements to assist part qualification.

This paper presents an LPBF superposition thermal model constructed with Short-Wave Infrared (SWIR) thermal camera measurements. A theoretical superposition model's derivation for pulsed laser LPBF reveals the methodology for experiment-based modeling. The superposition modeling process gauges the SWIR camera measurement's linearity. Processing simulation and experimental data with an in-situ framework evaluates the superposition model's ability to predict real thermal history variances.

Model Development

The theoretical pulsed laser superposition model's derivation follows Schwalbach et al.'s work for CW systems [6]. The pulsed laser's volumetric heat source model, $\dot{q}(x,y,z,t)$, is [7]

$$\dot{q}(x,y,z,t) = \frac{2(1-R)P}{\delta_p \pi \omega^2} \exp\left(-2\frac{x^2+y^2}{\omega^2}\right) \exp\left(-\frac{|z|}{\delta_p}\right) \left[1-\Theta(t-t_e)\right], \tag{1}$$

where (x,y,z) are the spatial coordinates, t is the time, R is the reflectance, P is the laser power, δ_p is the laser's optical penetration depth, ω is the beam waist, Θ is the Heaviside function, and t_e is the exposure time. The temperature field, $T(x,y,z,t)$, a single laser pulse produces in a semi-infinite domain is

$$T(x,y,z,t) = T_0 + \frac{2(1-R)P}{\delta_p \pi \rho c_p} \int_0^t \frac{\left[1-\Theta(t_0-t_e)\right]\Theta(t-t_0)}{8\alpha(t-t_0)+\omega^2} \exp\left(\frac{-2(x^2+y^2)}{8\alpha(t-t_0)+\omega^2}\right) \cdot \frac{1}{2} \left(\begin{array}{l} \exp\left(\frac{\alpha(t-t_0)-\delta_p z}{\delta_p^2}\right) \operatorname{erfc}\left(\frac{2\alpha(t-t_0)-\delta_p z}{\sqrt{4\alpha(t-t_0)}\delta_p}\right) \\ + \exp\left(\frac{\alpha(t-t_0)+\delta_p z}{\delta_p^2}\right) \operatorname{erfc}\left(\frac{2\alpha(t-t_0)+\delta_p z}{\sqrt{4\alpha(t-t_0)}\delta_p}\right) \end{array} \right) dt_0 , \tag{2}$$

where T_0 is the initial temperature and α is the thermal diffusivity. The relative temperature change, $T(x,y,z,t)-T_0$, is the laser pulse's basis function. The *x*-*y* plane radially symmetric basis function, $G(r,t)$, at $z = 0$ is

$$G(r,t)=\frac{2(1-R)P}{\delta_p \pi \rho c_p}\int_0^t \frac{\left[1-\Theta(t_0-t_e)\right]\Theta(t-t_0)}{8\alpha(t-t_0)+\omega^2}\exp\left(\frac{-2r^2}{8\alpha(t-t_0)+\omega^2}\right) \cdot \exp\left(\frac{\alpha(t-t_0)}{\delta_p^2}\right)\operatorname{erfc}\left(\frac{\sqrt{\alpha(t-t_0)}}{\delta_p}\right)dt_0 \quad , \tag{3}$$

where $r=\sqrt{x^2+y^2}$.

Superimposing single pulse basis function copies shifted in space and time simulates multiple laser pulses. The basis function copies offset spatially according to the laser scan path and temporally by the pulse period. The temperature for a multi-pulse simulation at $z = 0$ is

$$T(x,y,t)=T_0+\sum_{k=1}^{K} G_k(r,t'), \tag{4}$$

where G_k is the k^{th} laser pulse's basis function. The k^{th} pulse's radius, r, to a given (x,y) and its relative time, t', are

$$\begin{cases} r=\sqrt{\left(x-x_{0,k}\right)^2+\left(y-y_{0,k}\right)^2} \\ t'=t-t_{0,k} \end{cases} , \tag{5}$$

where $\left(x_{0,k}, y_{0,k}\right)$ are its exposure coordinates and $t_{0,k}$ is when exposure begins.

Figure 1 demonstrates superposition for six laser pulses (P = 200 W, t_e = 70 µs, ω = 70 µm, δ_p = 60 µm) striking 304L stainless steel (k = 15 W/m·K, ρ = 7800 kg/m^3, c_p = 500 J/kg·K). Figure 1 (a) contains the pulses' basis function profile plots (purple to red curves) at their relative times, offset in space by the laser point-to-point distance (60 µm). The profiles demonstrate the basis function's temperature magnitude decreases, and its waist increases after the exposure time as heat conducts away from the exposure location. Adding the pulses' temperatures at a particular spatial point produces that location's total temperature. Figure 1 (a) shows the final superposition result by a profile plot (black curve) from the 2D temperature map in Fig. 1 (b).

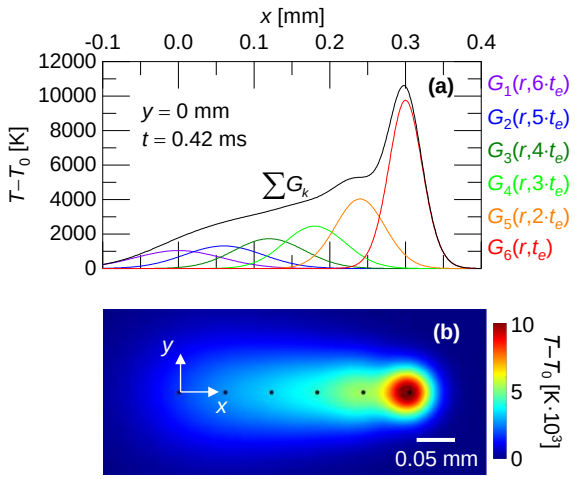

Fig. 1. (a) Theoretical laser pulse basis function profiles with resulting superposition temperature and (b) 2D temperature map with coordinate system and exposure points.

A matrix algebra approach equivalently provides the superposition results in Fig. 1. Equation 4 in matrix notation is

$$\vec{T} = T_0 + \boldsymbol{A}\vec{G}, \tag{6}$$

where $\vec{T}$ is the temperature vector, $\boldsymbol{A}$ is a matrix tracking the active basis function components for each (x, y, t), and $\vec{G}$ is the basis function vector. The laser's scan path and relative exposure time information build $\boldsymbol{A}$. Inverting Eq. 6 solves for an unknown basis function by utilizing known scan pathing and spatiotemporal temperature data like Fig. 1 (b). The temperature data's samplings in space and time can provide, but do not limit, the inverted basis function's radial and temporal resolutions. Equation 6's inversion yields $\vec{G}$ exactly for theoretical cases with a full rank $\boldsymbol{A}$.

Experimental Basis Function Inversion

A SWIR camara observing a Renishaw AM250 (pulsed laser) rastering a 5×5 mm^2, 50 µm thick, 304L stainless steel layer provides the spatiotemporal thermal data for basis function inversion. The camera samples at 3345.8 Hz with 130 µm/pixel and 135 µm/pixel x and y instantaneous field of views, respectively (see [8] for further details). The raw camera data corrects to temperature using a procedure like discussed in [9]. Figure 2 (a) shows a temperature corrected image with the laser's exposure points (white dots) and parameters annotated. The laser scans with a 0° rotation angle, a 60 µm point-to-point distance, d_p, and an 85 µm hatch spacing, d_h. Each image supplies an $\boldsymbol{A}$ sub-matrix and a $\vec{T}$ sub-vector. Since $\boldsymbol{A}$'s columns must equal $\vec{G}$'s length, the procedure builds $\boldsymbol{A}$ sub-matrices by assuming $\vec{G} \to 0$ after 10 ms, or beyond a radius of 0.78 mm. Also, the process assumes $\vec{G}$ has resolutions of Δt = 150 µs and Δr = 130 µm. Data from 500 consecutive thermal images assemble $\boldsymbol{A}$ and $\vec{T}$ to invert $\vec{G}$. Multiple images provide a full rank $\boldsymbol{A}$ and reduce $\vec{G}$'s noise. Least squares produces $\vec{G}$ with minimum error by

$$\vec{G} = \left(\boldsymbol{A}^T \boldsymbol{A} \right)^{-1} \boldsymbol{A}^T \left(\vec{T} - T_0 \right). \tag{7}$$

Figure 2 (b-d) contain the experimental basis function. The basis function's temperature magnitude decreases with increasing radius. For each radial component, the basis function's temperature magnitude quickly reaches a maximum, and then decreases with increasing time. Sampling rate variances and scan path location uncertainty cause the basis function's noise. The inversion success reveals the SWIR temperature data's linearity.

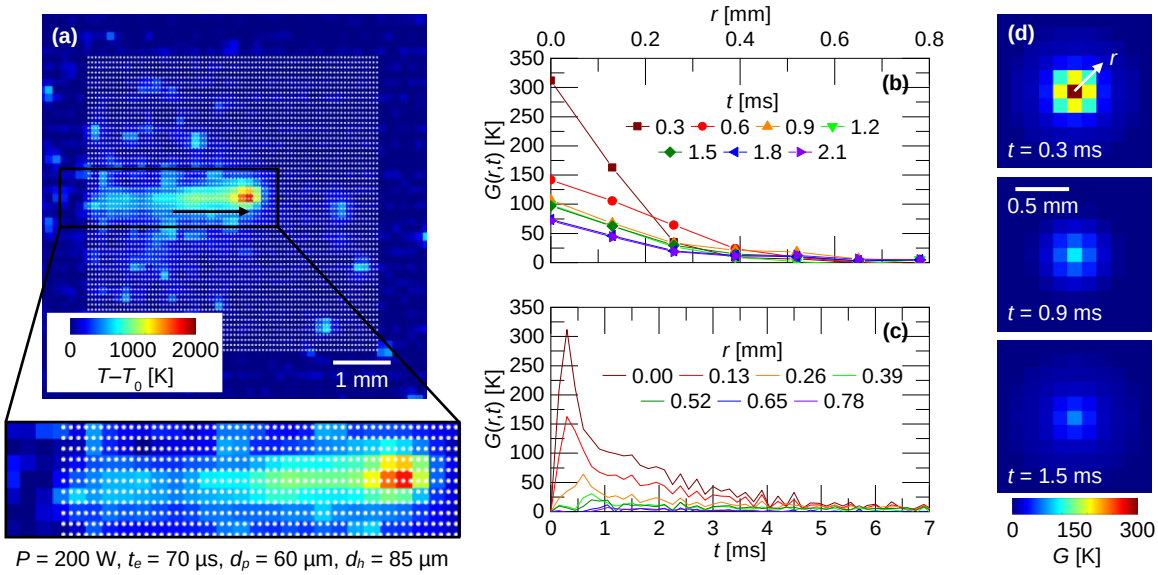

Fig. 2. (a) SWIR melt pool image with laser exposure points and experimental basis function (b) plotted as a function of radius for various times, (c) plotted as a function of time for all radial components, and (d) mapped for various times.

Simulation Results

The superposition model simulates the LPBF temperature field the SWIR camera measures by applying the experimental basis function in Eq. 6. The model predicts the 5×5 mm^2 layer's thermal history in 4 minutes (Dell OptiPlex 5050, Intel Core i-7700 CPU, 3.6 GHz). Figure 3 compares the superposition predictions with the layer's experimental temperature results. Figure 3 (a-c) show selected pixels' temporal data relative to their respective times at experimental maximum temperature. The data in Fig. 3 (a-c) illustrate thermal history differences arise when the laser progresses from a corner to the raster's middle. The superposition simulation predicts those differences with the root mean square errors (RMSE) annotated on Fig. 3 (a-c). The melt pool images in Fig. 3 (d-f) demonstrate the spatial temperature agreement between the experiment's measurements and the simulation's predictions.

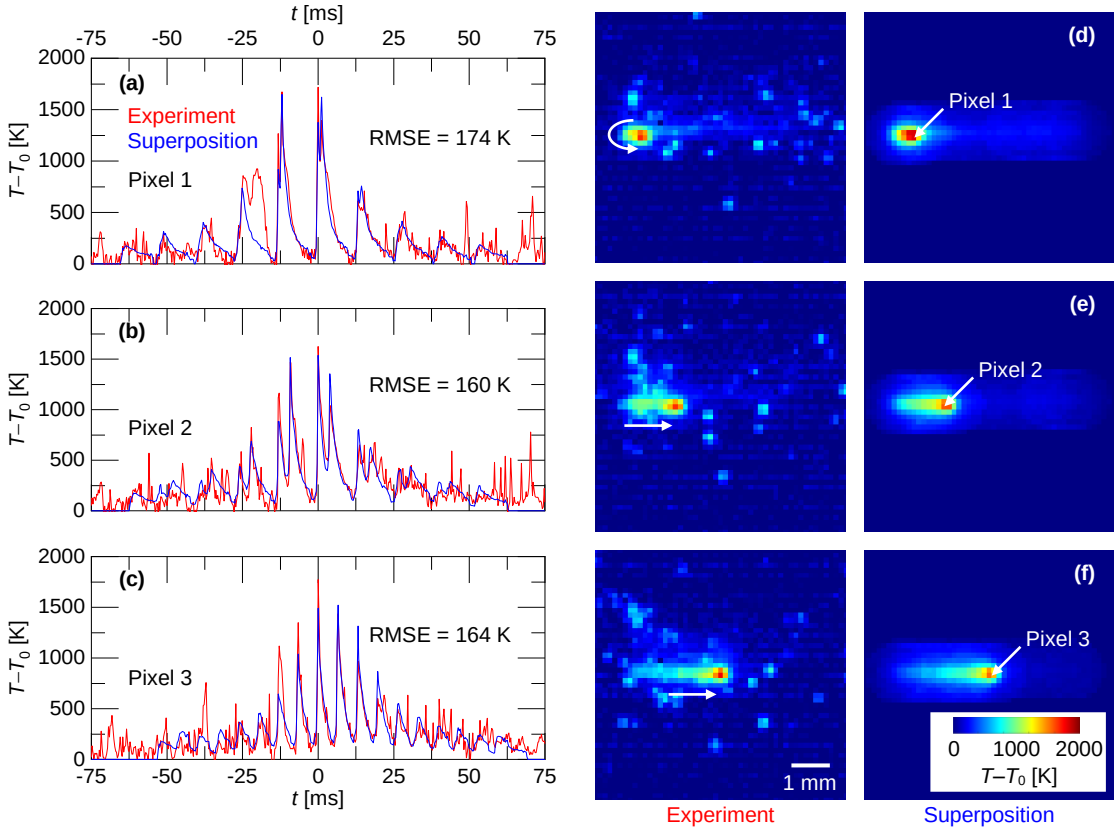

Fig. 3. Experiment and superposition simulation (a,b,c) temperature histories and (d,e,f) melt pool images for various locations along a laser raster in the 5×5 mm^2 layer.

Thermal features capture the layer's entire thermal history by compressing each pixels' temporal data to a single metric. This process produces a thermally based data map for layers. Thermal features have application in part property correlations and in-situ defect detection. A layer's thermal feature map also clearly show how the laser's scan path affects the thermal history. Two common thermal features are the maximum temperature [10] and the time above threshold [11]. Figure 4 evaluates the superposition simulation's predictions of those thermal features. Figure 4 contains experimental and simulated thermal feature profile plots and maps. The maximum temperature, T_{max}, predictions in Fig. 4 (a) and (c) match the experiments in the interior but deviate at the layer's edges. This suggests a linearity reduction where the laser corners. The entire layer's maximum temperature RMSE is 177 K. Figure 4 (b) and (d) illustrate the simulation successfully predicts the experimental time above threshold, τ. Time above threshold experimental deviations occur at some locations due to balling. The time above threshold prediction has a 1.2 ms RMSE.

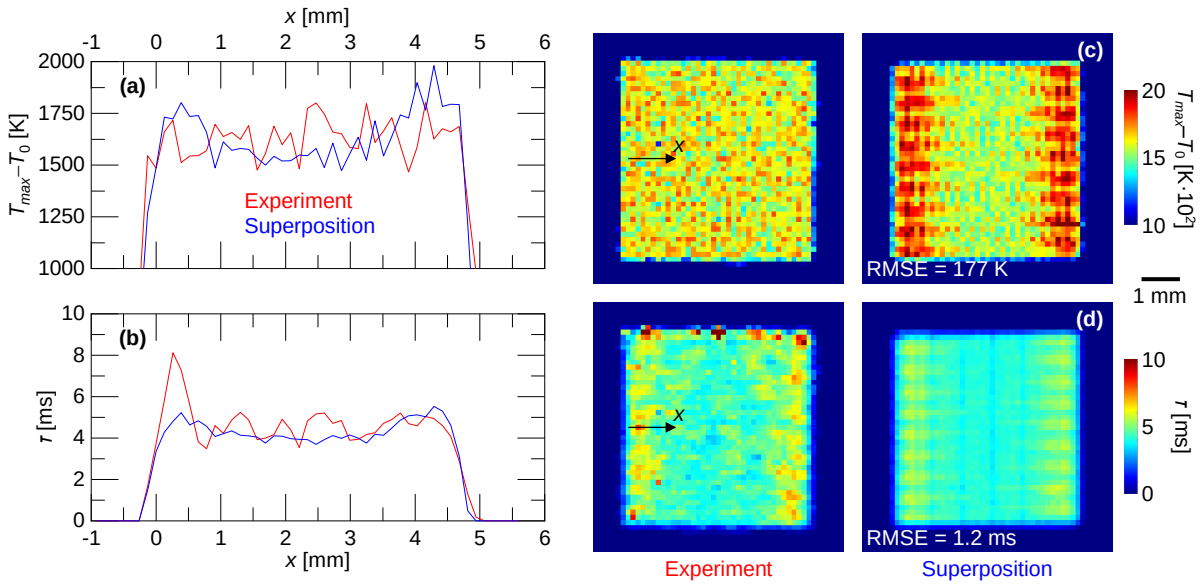

Fig. 4. Experiment and superposition (a) maximum temperature and (b) time above threshold profile plots from 2D (c) maximum temperature and (d) time above threshold maps.

Conclusions

Inverting a basis function (i.e. the temperature response from a single laser pulse) from SWIR camera data enables experiment-based superposition thermal modeling for LPBF. The successful basis function inversion demonstrates the SWIR camera temperature data's linearity for nominal manufacturing. The superposition approach simulates a simple 5×5 mm^2 layer in 4 minutes. The simulation's analyzed time series data fits the experiment's data with a maximum 174 K RMSE. Simulation thermal features track experimental results with a 177 K maximum temperature RMSE and a 1.2 ms time above threshold RMSE. The pulsed laser experimental superposition framework should adapt to CW LPBF systems since thermal cameras have finite sampling rates. The superposition model's applications include laser scan path effects prediction to baseline experimental data in part qualification, and feedforward controls. Future work will explore experimental superposition for various LPBF manufacturing cases and evaluate the ability to flag defects in parts.

Acknowledgement

This work was funded by Honeywell Federal Manufacturing & Technologies under Contract No. DE-NA0002839 with the U.S. Department of Energy. The United States Government retains and the publisher, by accepting the article for publication, acknowledges that the United States Government retains a nonexclusive, paid up, irrevocable, world-wide license to publish or reproduce the published form of this manuscript, or allow others to do so, for the United States Government purposes.

References

[1] Druzgalski CL, Ashby A, Guss G, King WE, Roehling TT, Matthews MJ. Process optimization of complex geometries using feed forward control for laser powder bed fusion additive manufacturing. Addit Manuf 2020;34:101169. https://doi.org/10.1016/j.addma.2020.101169.

[2] Ning J, Sievers DE, Garmestani H, Liang SY. Analytical modeling of part porosity in metal additive manufacturing. Int J Mech Sci 2020;172:105428. https://doi.org/10.1016/j.ijmecsci.2020.105428.

[3] Bruna-Rosso C, Demir AG, Previtali B. Selective laser melting finite element modeling: Validation with high-speed imaging and lack of fusion defects prediction. Mater Des 2018;156:143–53. https://doi.org/10.1016/j.matdes.2018.06.037.

[4] Khairallah SA, Anderson AT, Rubenchik A, King WE. Laser powder-bed fusion additive manufacturing: Physics of complex melt flow and formation mechanisms of pores, spatter, and denudation zones. Acta Mater 2016;108:36–45. https://doi.org/10.1016/j.actamat.2016.02.014.

[5] Moran TP, Li P, Warner DH, Phan N. Utility of superposition-based finite element approach for part-scale thermal simulation in additive manufacturing. Addit Manuf 2018;21:215–9. https://doi.org/10.1016/j.addma.2018.02.015.

[6] Schwalbach EJ, Donegan SP, Chapman MG, Chaput KJ, Groeber MA. A discrete source model of powder bed fusion additive manufacturing thermal history. Addit Manuf 2019;25:485–98. https://doi.org/10.1016/j.addma.2018.12.004.

[7] Mishra AK, Aggarwal A, Kumar A, Sinha N. Identification of a suitable volumetric heat source for modelling of selective laser melting of Ti6Al4V powder using numerical and experimental validation approach. Int J Adv Manuf Technol 2018;99:2257–70. https://doi.org/10.1007/s00170-018-2631-4.

[8] Lough CS, Wang X, Smith CC, Landers RG, Bristow DA, Drallmeier JA, et al. Correlation of SWIR imaging with LPBF 304L stainless steel part properties. Addit Manuf 2020;35:101359. https://doi.org/10.1016/j.addma.2020.101359.

[9] Lane B, Moylan S, Whitenton EP, Ma L. Thermographic measurements of the commercial laser powder bed fusion process at NIST. Rapid Prototyp J 2016;22:778–87. https://doi.org/10.1108/RPJ-11-2015-0161.

[10] Krauss H, Zeugner T, Zaeh MF. Layerwise monitoring of the Selective Laser Melting process by thermography. Phys Procedia 2014;56:64–71. https://doi.org/10.1016/j.phpro.2014.08.097.

[11] Mohr G, Altenburg SJ, Ulbricht A, Heinrich P, Baum D, Maierhofer C, et al. In-situ defect detection in laser powder bed fusion by using thermography and optical tomography—comparison to computed tomography. Metals (Basel) 2020;10. https://doi.org/10.3390/met10010103.